

Observational constraints to the dynamics of dust particles in the coma of comet 67P/Churyumov-Gerasimenko

Frattin E.,¹★ Bertini I.,^{2,3} Ivanovski S.L.,⁴ Marzari F.,¹ Fulle M.,⁴ Zakharov V.V.,^{2,3} Moreno F.,⁵ Naletto G.,¹ Lazzarin M.,¹ Cambianica P.,⁶ Cremonese G.,⁶ Ferrari S.,⁷ Ferri F.,⁷ Güttler C.,⁸ La Forgia F.,^{1,2} Lucchetti A.,⁶ Pajola M.,⁶ Penasa L.,⁷ Rotundi A.,^{2,3} Sierks H.,⁸ Tubiana C.^{3,8}

¹ Dipartimento di Fisica e Astronomia G. Galilei, Università di Padova, Vicolo dell'Osservatorio 3, 35122 Padua, Italy.

² Dipartimento di Scienze e Tecnologie, Università di Napoli "Parthenope", CDN, IC4 80143 Naples, Italy.

³ Institute for Space Astrophysics and Planetology (IAPS)-INAF, Via Fosso del Cavaliere 100 00133 Rome, Italy.

⁴ Osservatorio Astronomico di Trieste, Istituto Nazionale di Astrofisica, Via G.B. Tiepolo, 11 I-34143 Trieste, Italy.

⁵ Instituto de Astrofísica de Andalucía, CSIC, Granada 18008, Spain.

⁶ Osservatorio Astronomico di Padova, Istituto Nazionale di Astrofisica, Vicolo dell'Osservatorio 5, 35122 Padua, Italy.

⁷ Center of Studies and Activities for Space (CISAS) G. Colombo, University of Padova, Via Venezia 15, 35131 Padua, Italy.

⁸ Max Planck Institute for Solar System Research, Justus-von-Liebig-Weg 3, 37077 Göttingen, Germany.

Accepted XXX. Received YYY; in original form ZZZ

ABSTRACT

In this work we aim to characterise the dust motion in the inner coma of comet 67P/Churyumov-Gerasimenko to provide constraints for theoretical 3D coma models. The OSIRIS camera on board the Rosetta mission was able for the first time to acquire images of single dust particles from inside the cometary coma, very close to the nucleus. We analyse a large number of particles, performing a significant statistic of their behaviour during the post perihelion period, when the spacecraft covered distances from the nucleus ranging between 80 and 400 km. We describe the particle trajectories, investigating their orientation and finding highly radial motion with respect to the nucleus. Then, from the particle brightness profiles, we derive a particle rotational frequency of $\nu < 3.6$ Hz, revealing that they are slow rotators and do not undergo fragmentation. We use scattering models to compare the observed spectral radiance of the particles with the simulated ones in order to estimate their size, finding values that range from millimetres up to centimetres. The statistics performed in this paper provide useful parameters to constrain the cometary coma dynamical models.

Key words: comets: individual – methods: data analysis – techniques: photometric, image processing

1 INTRODUCTION

The cometary coma is a complex environment where several physical and chemical processes regarding solid and gaseous materials emitted from the nucleus take place, such as fragmentation, sublimation and photoionization. Many models of different levels of complexity have been developed during the years in order to describe the cometary dust motion (Crifo et al. 2005; Zakharov et al. 2009; Marschall et al. 2016; Ivanovski et al. 2017a). The main forces that govern the motion of the particles in the vicinity of the nucleus are the gravitational force exerted by the comet, the aerodynamical force generated by the gas drag, the solar gravity as well as the solar

radiation pressure.

The gas is considered to be the main driver of the motion up to a certain distance from the nucleus at which the dust particles reach their terminal velocity decouple from the gas, which occurs at about 10 nucleus radii from the center of mass (Crifo et al. 2002, 2005; Zakharov et al. 2018). Fulle et al. (2015) and Ivanovski et al. (2017a) computed the exact distances where single particles reach their terminal velocity for 67P/Churyumov-Gerasimenko (hereafter 67P), obtaining values that range between 10 to 100 km depending on the gas field, the mass and density of the particles. The gas production rate governs the release process and it changes along the comet trajectory before and after perihelion.

In general, since drag and gravity decrease with the distance from the nucleus, at a certain height the solar pressure force finally dom-

★ E-mail: elisa.frattin@unipd.it

inates: this may happen either close or far from the nucleus, depending on the particular case (Moreno et al. 2017; Ivanovski et al. 2017a; Skorov et al. 2018).

Furthermore, the shape of the particles plays an important role in the dynamical models. The up-to-date observational data revealed limitations of the models which assume sphericity of dust grains. Indeed, the evidence of irregular shape of dust particles was revealed by the Stardust mission, by the IDPs (Interplanetary Dust Particles) analysis (Rotundi et al. 2007, 2008) and by the measurements obtained by the Grain Impact Analyzer and Dust Accumulator (GI-ADA, (Colangeli et al. 2007; Della Corte et al. 2014)) and Cometary Secondary Ion Mass Analyzer (COSIMA, (Le Roy et al. 2015)) for the Rosetta mission (Langevin et al. 2016; Fulle & Blum 2017; Ivanovski et al. 2017a). The images provided by the Optical, Spectroscopic, and Infrared Remote Imaging System (OSIRIS, (Keller et al. 2007)) revealed indications of rotational motion of particles by the brightness variation in the tracks of single particles, interpreted as rotational motion of non-spherical particles (Fulle et al. 2015; Frattin et al. 2017).

Therefore refined models, based on the use of aspherical particles, have been developed by Ivanovski et al. (2017a) and Skorov et al. (2016).

All the aforementioned models dealing with dust dynamics in the inner coma need to be verified, tested, and refined through observational data. It is therefore of pivotal importance to use Rosetta data to constrain theoretical interpretations providing inputs to the models. During orbiting around comet 67P, the OSIRIS camera on board the Rosetta spacecraft (Keller et al. 2007) was able to acquire images from inside the cometary coma, close to the nucleus. In July 2015 - January 2016 time frame, the spacecraft was at distances between 80 km and 400 km from the nucleus (with one configuration at 1200 km). For the first time, it was possible to directly observe tracks of single dust particles and measure their light curve, to determine hints on their rotational state, and size, providing a good statistics of the aforementioned parameters, thanks to the huge amount of data collected.

In this work we present an extensive analysis of dust particles characteristics and dynamics. In Section 2 we describe the dataset. In Section 3 we show the observational evidence of the radial motion of the dust particles, in Section 4 we present a statistic of the rotational frequency of the particles in the inner coma of the comet. Afterwards, we give an estimate of their shape evaluating their flattening.

In Section 5 we provide a photometric analysis of the dust particles deriving their size. A description of the rotational dynamics of the dust is given in Section 6. The conclusions are given in Section 7.

2 DATA

To study the direction of motion and the rotational state of the particles we used images acquired from August 2015 to January 2016 (the perihelion passage was in August 2015) by the OSIRIS Narrow Angle Camera (NAC) in the Orange filter ($\lambda = 649$ nm), with an exposure time of 12.5 seconds.

For the analysis we used 92 radiometric calibrated and geometric distortion corrected OSIRIS Level 3 and 3B (CODMAC L4) images¹. Details about the data processing, including all calibration steps

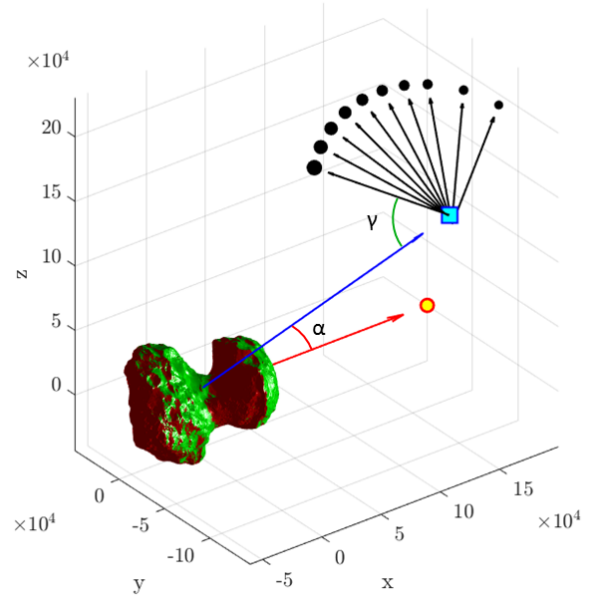


Figure 1. Example of the observational configuration of the set of images described in Table 2, the case of STP 081 GRAIN_COLOR_002. The red arrow represents the direction of the Sun (yellow circle). The black arrow represents the line of sight of the camera (cyan square) for each image, while the black circles stand for the dust particles. The line of sight lies on a plane perpendicularly to the plane containing the Sun, the comet and the s/c.

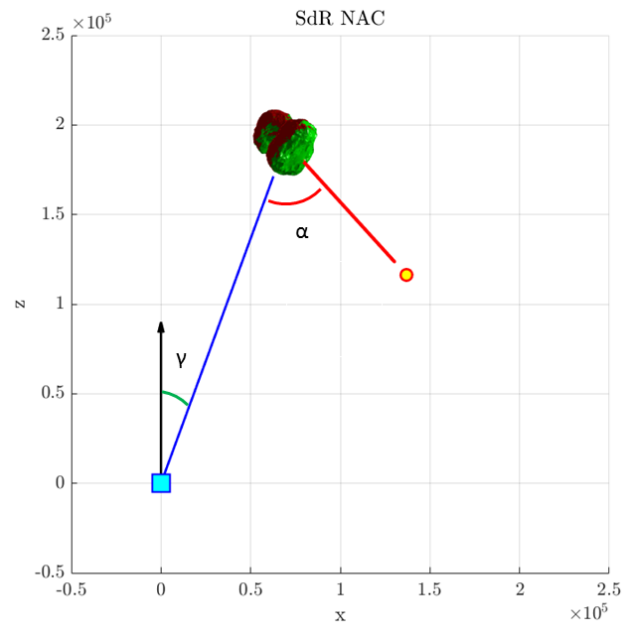


Figure 2. Example of the observational configuration of the set of images described in Table 3, the case of STP 081 GRAIN_TRACK_003. The red arrow represents the direction of the Sun (yellow circle). The black arrows represent the line of sight of the camera (cyan square). The line of sight lies on the plane containing the Sun, the comet and the s/c.

¹ The data are available at the Planetary Science Archive of the European Space Agency under <https://www.cosmos.esa.int/web/psa/rosetta>

applied to the images, can be found in [Tubiana et al. \(2015\)](#). The only difference between the used image levels is solely the unit: OSIRIS Level 3 images are in $\text{W}/(\text{m}^2 \text{ sr nm})$ while L3B images are I/F, thus unity.

During the entire mission, we regularly acquired sequences of images named dust particle track and dust particle colour, which were designed to study the motion and the colours, respectively, of individual particles in the dust coma. The design of those sequences was the same thorough the mission, allowing to combine data acquired at different epochs.

In this work we analyse both type of sequences. The activity name of each sequence is listed in Tables 2 and 3. At the time of the observations, the Rosetta spacecraft was at a distance from the nucleus between 84 and 437 km. The Rosetta +Z-axis, which is aligned with the camera boresight direction, was off-pointing with respect to the nucleus, which is therefore outside the camera field of view. To study the direction of the dust motion, in Section 3, we have analysed 28 images belonging to 5 sets of images listed in Table 1. The nucleus phase angle α (i.e. the angle between the direction of Sun and the direction of spacecraft as seen by the nucleus) is reported here for geometrical purposes and in these images is always less than 90° , hence the spacecraft is located in the day side of the coma, see Figure 1.

The plane of sight is perpendicular to the plane defined by the Sun, the nucleus and the spacecraft and these planes intersect at the line given by the direction between the Sun and the spacecraft. Therefore, the plane of sight contains the Sun. The images elongation ϵ (i.e. the angle between the direction of the line of sight and the direction of the Sun as seen by the spacecraft) changes within the sequence from the solar direction toward the anti-solar direction, from 50° to 160° . It means that the camera points dust that scatters from the forward direction up to the backward direction with respect to the Sun. This allows to investigate different parts of the coma at the same epoch. The phase angle of the dust follows the relation $\alpha_{\text{dust}} = 180^\circ - \epsilon$.

To study the rotational state and the photometry of the dust particles, in Section 4 and 5, we have analysed 64 images belonging to 7 sets of images taken in various epochs, listed in Table 3. We decided to focus on sets of images where the observational geometry configuration formed by the spacecraft, the comet, and the Sun remained constant. This means that the phase angle α , the elongation of the Sun ϵ and the angle γ (i.e. the angle between the direction of the spacecraft and the direction of the line of sight) are fixed within the observational series, see Figure 2. In this way, the condition of illumination of the particles during the time interval of a series is the same.

2.1 Detection method

The OSIRIS NAC camera is able to observe single dust particles in the coma of 67P. Each particle draws a track on the plane of the image, due to its motion during the exposure time. Therefore, the track is the 2D projection on the CCD focal plane of the 3D particle motion. We use the automatic method developed by [Frattin et al. \(2017\)](#) to detect the tracks from the images and to provide some photometric and geometric parameters, as their radiance, full width half maximum (FWHM) and orientation.

Figure 3 shows an example of an OSIRIS image with dust tracks, while Figure 4 illustrates the final step of the detection process in which the tracks are identified with a green line and a number. The method is based on a similarity function that evaluate the correspondence between two images. A set of synthetic tracks is generated,

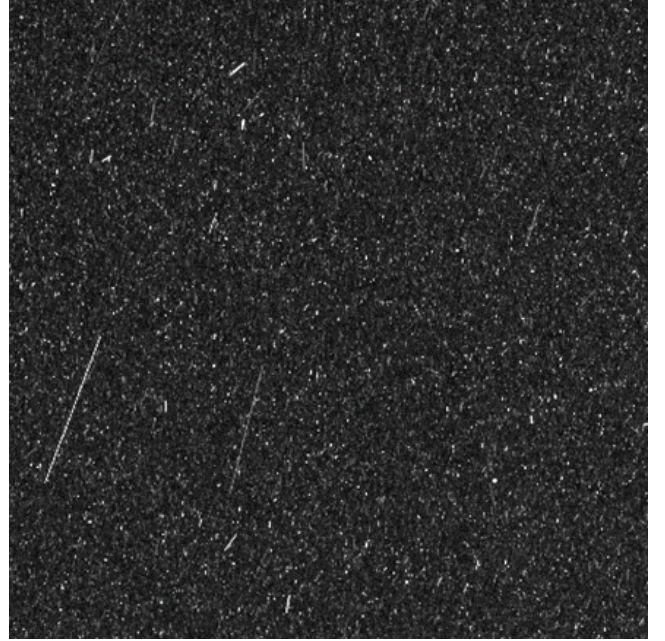


Figure 3. Image taken by NAC on 30 November 2015 at UT 19:25:04.078, belonging to STP 084. The colour scale follows a square root variation. The grey scale goes from black to white, which correspond to flux values of 0 and $0.000185 \text{ W}/(\text{m}^2 \text{ nm sr})$, respectively. The size of the image is 440×440 px.

characterised by their orientation and FWHM, given by the convolution of a rectangular function with a bi-dimensional Gaussian. Then, the Normalised Cross Correlation allows to evaluate the similarity between the features identified on a local zone of the images and the synthetic tracks generated. Eventually the length of the tracks, their position, orientation, flux and FWHM are provided. The flux is computed subtracting the background which is evaluated considering a rectangular area around the track, with sides parallel to the sides of the image and with length and height 10 pixel longer than the projection of the track on the two dimensions, in order to include the track properly.

3 TRANSLATIONAL MOTION OF THE DUST

In this section, we study the translational motion of the dust in the inner coma of comet 67P. We measure the particles direction of motion and we compare it with the trajectories computed by an appropriate dynamical model, in order to describe the inner coma dust motion. The data set consists in the post-perihelion images reported in Table 2, which geometry is described in Section 2.

3.1 Method

To measure the direction of motion of the dust particles we evaluate the angles shown in Figure 5. The angle δ is defined between the velocity vector of the particle on the plane of the image, (defined by the track itself) and the projected position vector of the nucleus on the plane of the image, in the NAC reference system, while the angle β is defined between the projection of the velocity vector of the particle on the plane of the image, and the projected position vector of the Sun.

The positions of the Sun and of the nucleus are derived using the

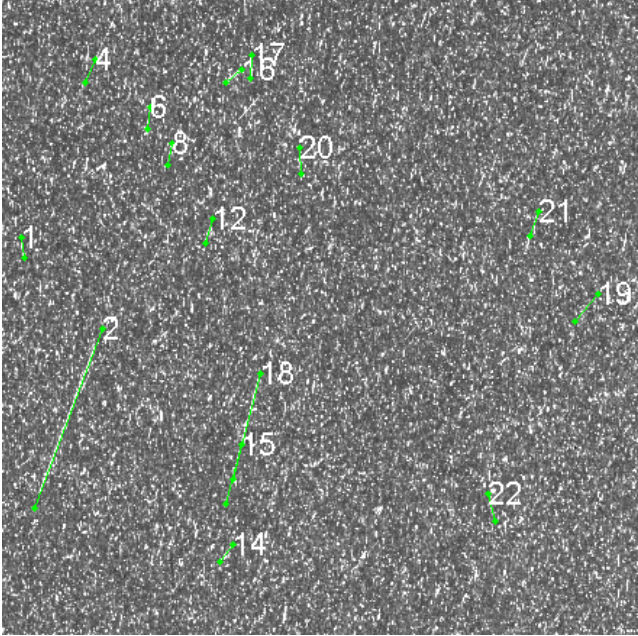


Figure 4. Last step of the detection process on image taken by NAC on 30 November 2015 at UT 19:25:04.078. The tracks are identified with a number and highlighted in green. The colour scale follows a square root variation.

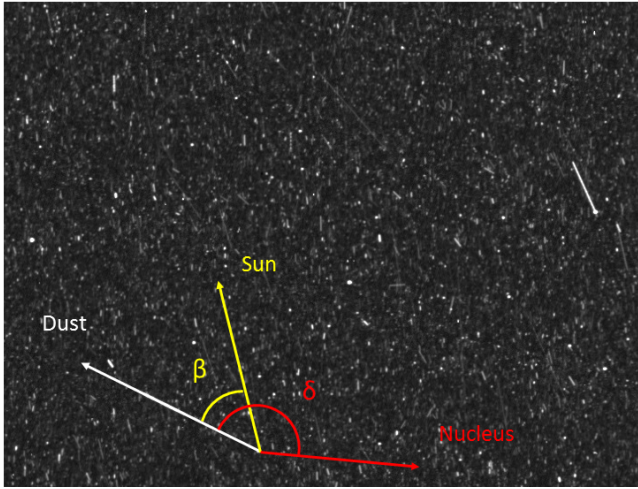


Figure 5. Single NAC image taken on 30 November 2015, STP 084, at UT 18:51:43.22. The image shows the construction of the position vectors used to compute the direction of motion of the dust. The track generated by the passage of a dust particle in the coma is shown in white, the unit vector of the position of the Sun in yellow and the unit vector of the position of the nucleus in red. The colour scale follows a square root variation. The grey scale goes from black to white, which correspond to flux values of 0 and 0.000035 W/(m² nm sr), respectively. The size of the image is 722x541 px.

SPICE Kernels (Acton 1996) and eventually, the cosine of the angles δ and β are computed. It is important to notice that the observational configuration changes within a single set of images. The elongation varies so the region of the coma investigated changes too.

3.2 Measurements

We measure the direction of motion of the particles observed in the images taken in the post perihelion period ranging from September

to November 2015. The results for the set STP 075 are shown in Figure 6. The results for the other set of images are reported in Appendix A. Each histogram represents the values of the cosine of the angle δ that each particle detected in a single image forms with the nucleus position vector. The elongation (ϵ) changes within a set, following the values illustrated in Table 2.

When the value of $\cos(\delta)$ is close to 1, the particle track, representing the projection of the motion on the plane of the image, is almost parallel to the direction vector of the nucleus. Our analysis shows that the majority of the particles have a value of $\cos(\delta)$ very close to 1, proving that the dust motion is mainly radial to the nucleus. Therefore, the bulk of dust aggregates comes directly from the nucleus while the small deviations are probably generated by a population of dust inbound orbits around the nucleus (Bertini et al. 2019).

3.3 Model

We developed a simple model of dust dynamics in the region where dust is completely decoupled from the gas. It is assumed that at the entrance in this region the dust particles have some initial velocity and further their motion is governed by the solar gravitational force, the solar radiation pressure and the nucleus gravitational force.

We consider a static model in which the heliocentric distance of the nucleus and of the spacecraft are constant, justified by the short interval of time (hours) with respect to the heliocentric motion of the comet in which the ejection events occurred. The distance between the spacecraft and the nucleus is also constant.

The gravitational force of the Sun is defined as follows:

$$F_{G\odot} = \frac{GM_{\odot}}{r_{\odot}^2} m_p \quad (1)$$

where $m_p = \frac{4\pi\rho_d r^3}{3}$ is the mass of the particle, ρ_d is the density of the particle and r the radius. $r_{\odot} = (1.496 \cdot 10^{11} r_h)$ is the heliocentric distance in metres.

The radiation pressure is:

$$F_{rad} = \frac{F_{\odot}}{r_h^2} \frac{Q_{pr} \pi r^2}{c} \quad (2)$$

where F_{\odot} is the Sun radiation intensity at 1 AU (corresponding to $F_{\odot} = 1360 \text{ W/m}^2$), c is the speed of light, and Q_{pr} is the scattering efficiency for radiation pressure ($Q_{pr} = 1$ for total reflecting particles).

The gravitational force of the nucleus is:

$$F_g = \frac{GM_N}{r_c^2} m_p \quad (3)$$

where $M_N = 10^{13} \text{ kg}$ is the mass of the nucleus (Pätzold et al. 2016), and r_c is the distance of the particle from the nucleus.

We simulate an initial momentum spread isotropically from 10 km from the surface of the nucleus, which is the distance at which the drag force becomes negligible. The velocity is defined in the nucleus reference system as:

$$\begin{cases} v'_x = v_0 \sin \theta \cos \phi \\ v'_y = v_0 \sin \theta \sin \phi \\ v'_z = v_0 \cos \theta \end{cases}$$

where v_0 is the initial velocity value, $\theta \in [0, \pi]$ is the polar angle and $\phi \in [0, 2\pi]$ is the azimuthal angle.

We compute the trajectories travelled by dust particles of radius

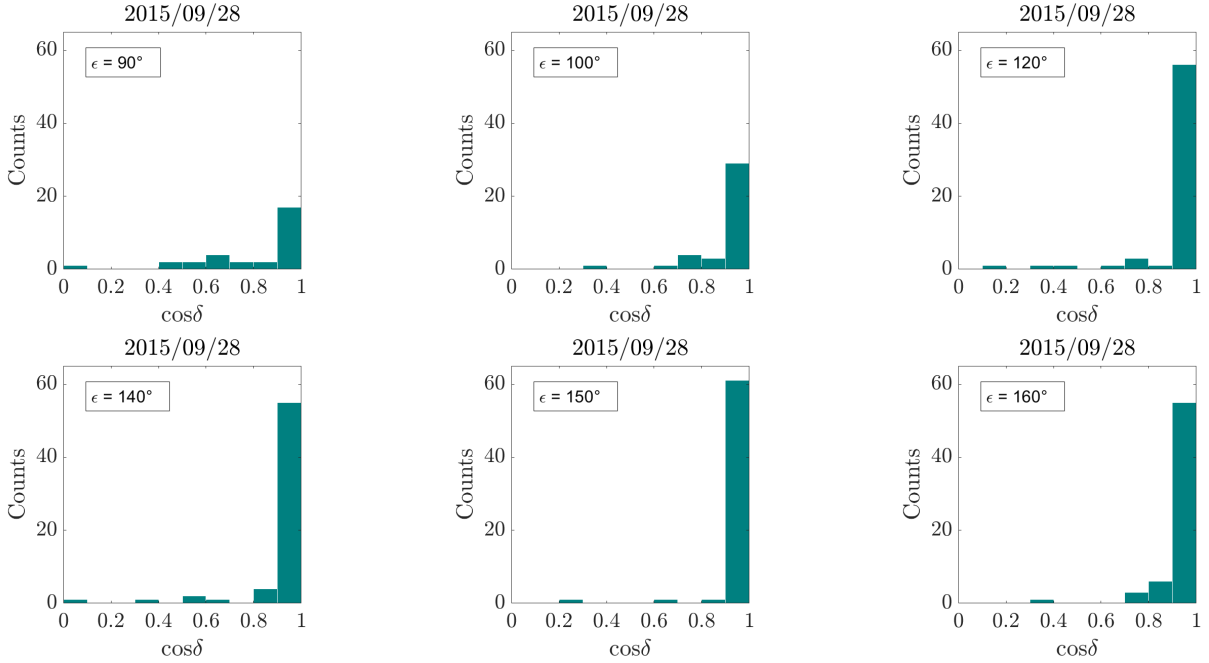


Figure 6. The histograms show the value of the cosine of the angle δ between the velocity vector of the particle on the image plane, and the projected position vector of the nucleus on the plane of the image, in the NAC reference system, for the set STP 075 GRAIN_COLOR_002.

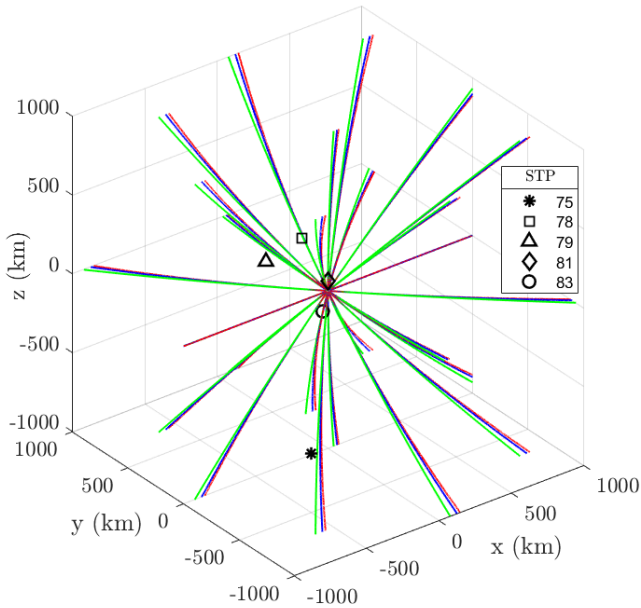


Figure 7. The figure shows the 3D trajectories of the dust particles ejected from the nucleus in all direction isotropically. The colour code is the following: green for particles of 0.1 mm and $v = 20$ m/s, blue for particles of 1 mm and $v = 5$ m/s and red for particles of 10 mm and $v = 1.5$ m/s. Also the s/c position at each STP is shown.

ranging from 0.1 mm to 10 mm. The model depends on the density of the dust ρ_d , the distance from the Sun r_h and the initial velocity vector v_0 .

We set $\rho_d = 800 \text{ kg/m}^3$ (Fulle et al. 2016b) and $r_h = 1.37 \text{ AU}$ as in the case of the set of images STP 075 taken just after the perihelion. The initial velocity is $v = 20, 5$ and 1.5 m/s, respectively, for particles of 0.1, 1 and 10 mm, based on GIADA and OSIRS measurements

of Della Corte et al. (2016) and Ott et al. (2017) and on the work of Ivanovski et al. (2017a). We note that the dust velocity may depend on the direction from where the particle comes. Therefore, in our simple model with isotropic ejection of particles, we use some averaged velocities. The dust particles undergo the solar radiation pressure in different ways, depending on their size and mass. The smaller the particle the stronger the effect of the solar radiation pressure. At the same time, the small particles have higher initial velocities (due to acceleration by the gas). The combination of these parameters result in an almost radial motion of all particle size ranges considered. Figure 7 shows the 3D trajectories of the particles of 0.1 mm, in green, of 1 mm in blue and of 10 mm in red. The Sun lies on the negative branch of the x-axis and the nucleus of 67P is located at the origin of the axis. The black symbols represent the position of the s/c in the five epochs. The plane in which the camera is pointing is always perpendicular to the plane formed by the Sun, the nucleus and the spacecraft. Following this model we find that the motion is almost radial in the inner part of the coma of the comet 67P for this range of particle sizes and initial velocities.

4 ROTATIONAL STATE OF DUST PARTICLES

In this section, we present the analysis performed on particles that show evidence of rotation. We refer to the data set of Table 3. First, we measure the rotational frequency of the particles, then we evaluate their flattening, giving some information about their shape.

4.1 Method

We observe that some tracks show periodic variations in brightness, interpreted as rotational motion of the single dust particle. Figure 8 shows an example of light curve of a rotating particle. As a comparison, Figure 9 shows a light profile with irregular radiance variations below the level of the background that can not be considered as

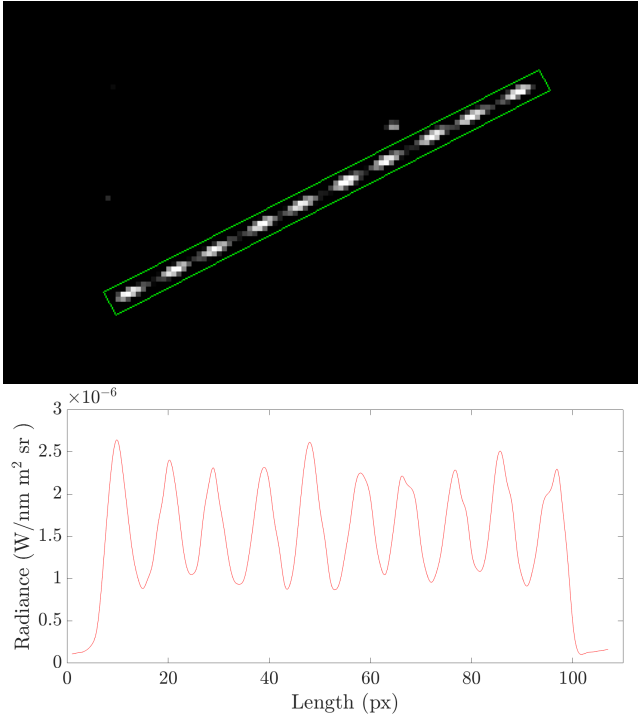


Figure 8. A rotating particle extracted from a single NAC image taken on 17 December 2015, STP 087, at UT 01:51:40.319 (top panel) and its brightness profile (bottom panel). The size of the image is 120x70 px.

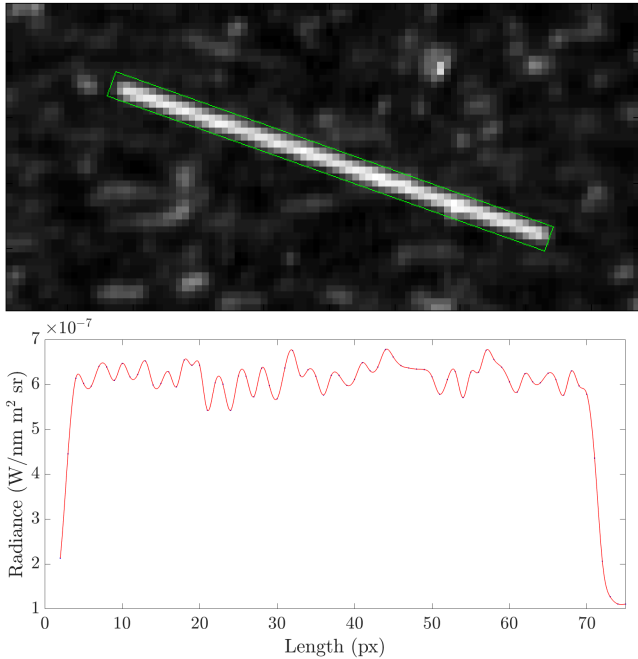


Figure 9. A particle that does not show evidence of rotation extracted from a single NAC image taken on 17 December 2015, STP 087, at UT 02:31:40.068 (top panel) and its brightness profile (bottom panel). The size of the image is 100x50 px.

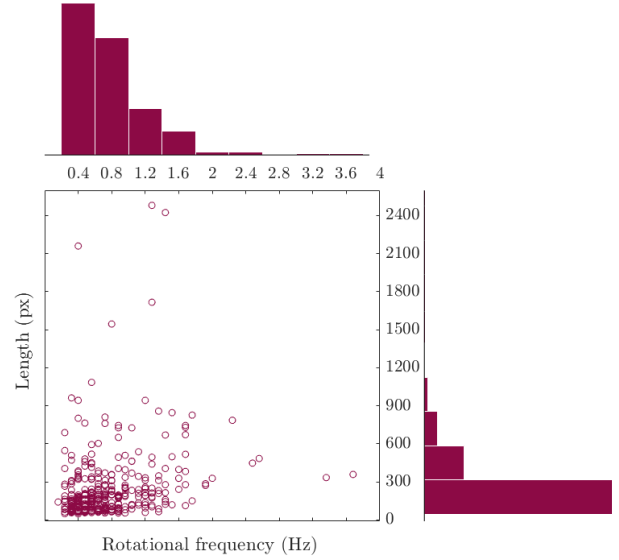


Figure 10. The figure shows the distribution of the particles in the parameter space defined by the tracks length (in px) and the rotational frequencies with their respective histograms.

evidence of rotation. We evaluate each track to distinguish between rotating particles and those that do not show evidence of rotation. We assume ellipsoidal particles with uniaxial rotation. We consider the three rotational modes around the main axis both for the prolate and oblate particles. Depending on the modes of rotation the track generated by the passage of the particle in the field of view shows brightness variation or not. For instance, an oblate spheroid rotating around its major axis perpendicular to the line of sight generates two peaks of brightness at each rotation, while if it rotates around its minor axis or around its major axis but parallel to the line of sight, it generates a homogeneous track. Consequently, the latter can not provide information about the particles shape. We use a criterion to classify the particles as rotating or not: the amplitude between the maximum and the minimum signal must be larger than the background signal. We discard those tracks that show only two peaks of brightness, in order to avoid possible contamination from two different tracks (Fulle et al. 2015). Overall, we detect 1916 particles of which 344 show a periodical light curve that corresponds to 18% of the whole population.

4.2 Rotational frequency

In approximation of uniaxial rotation of ellipsoidal particles with smooth homogeneous surface, the rotational frequency is straightforwardly computed dividing the number of maximum brightness peaks in the light curves for the exposure time. It does not depend on the track length, neither on the track distance nor the radiance, but only on the number of peaks. Hereafter the rotational frequency refers to the brightness frequency. Nevertheless, the statistics are affected by a bias due to the fact that only the longest tracks can provide fast rotations. Therefore, in order not to underestimate the high frequencies, we weight each track by its length, following Fulle et al. (2015). The probability of obtaining a specific rotational frequency is given by the formula $p_n = f_n \cdot l_n / \sum_{i=1}^N l_i$, where f_n is the rotational frequency of the particle, l_n is the length of the track and N is the total number of tracks in the image. In Figure 10

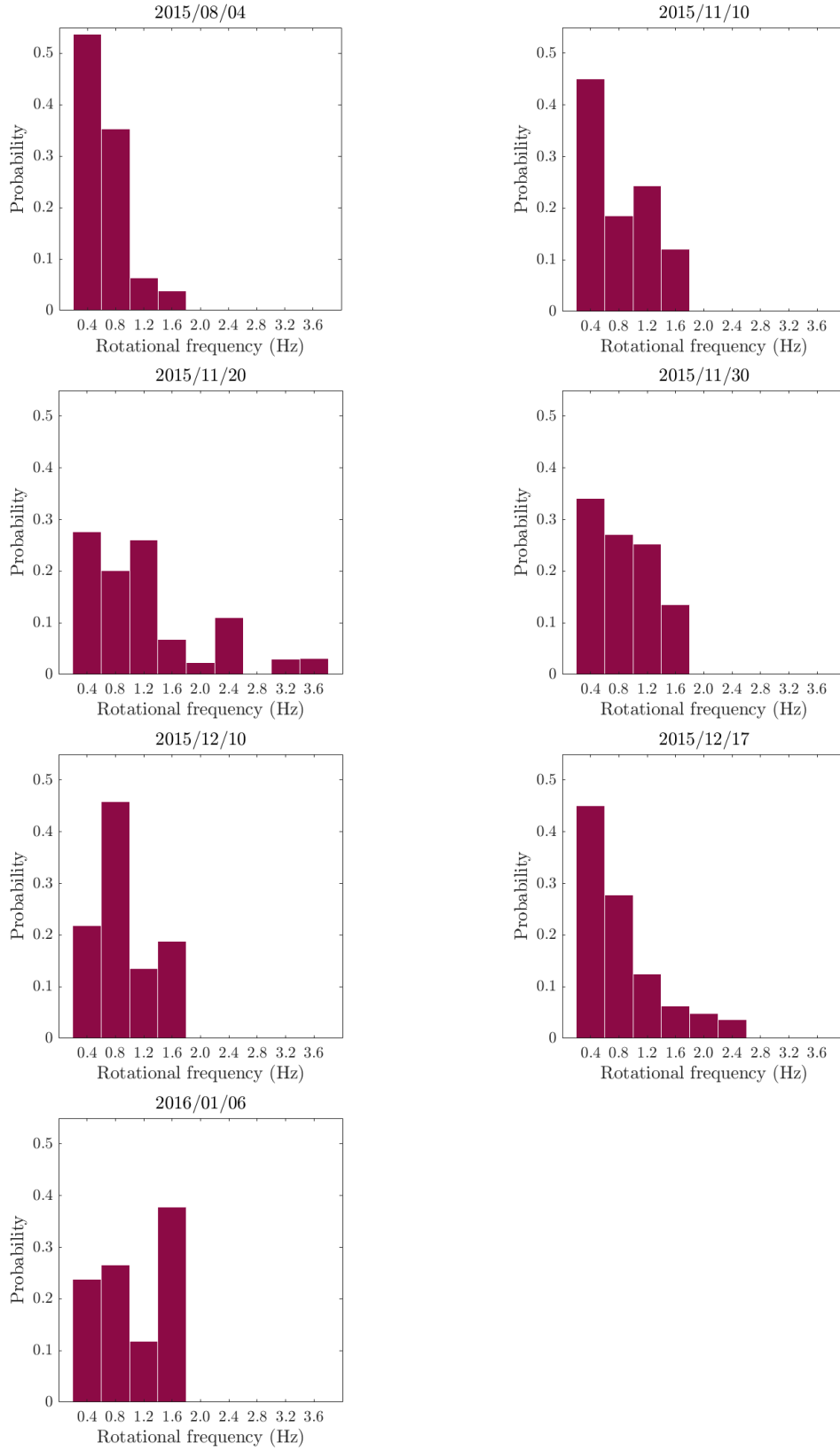


Figure 11. The histograms represent the rotational frequency distribution of the particles detected in the images listed in Table 3.

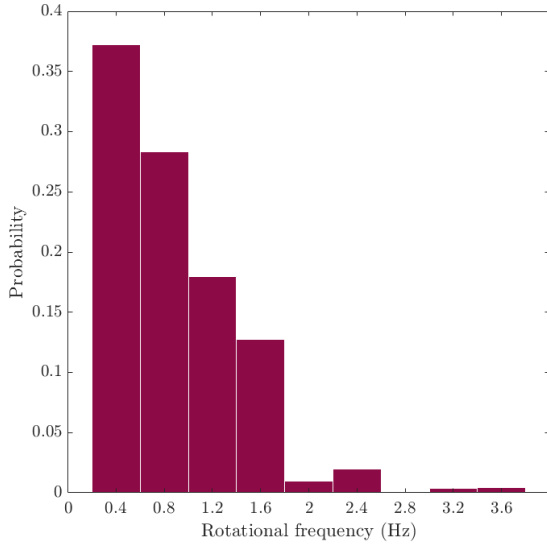


Figure 12. The histogram represents the distribution of the rotational frequency of the whole sample of particles reported in Table 3.

the length-frequency parameter space is shown. Furthermore, we correct for the projection effect. Since the trajectories are almost radial, as shown in the previous section, we can approximate the angle they form with the line of sight to the angle γ shown in Table 3. Therefore, the final length of a track (l_n) is equal to the length observed divided by the sine of the angle gamma. In Figure 11 we report the distribution of the rotational frequencies weighted for the length of the tracks for the entire sample of particles detected in every single daily set.

All the images sets show a higher probability to find slow rotating particles rather than fast ones. Moreover, the decreasing trend is common to all sets of images taken at different epochs and at different nucleocentric distances. This suggests that we are looking at a population of dust particles that did not undergo significant morphological and dimensional changes after their ejection from the nucleus. Therefore, a cumulative study of the data is allowed. In Figure 12, the distribution of the rotational frequencies of the whole set of images is merged in one single histogram. It results in a clear decreasing trend from 0.4 ± 0.2 up to a maximum of 3.6 ± 0.2 Hz, where the uncertainty corresponds to the bin sensitivity. About 40% of the particles have frequencies between the minimum value of 0.24 Hz (corresponding to three peaks of brightness) and 0.56 Hz (corresponding to seven peaks of brightness).

These values are in agreement with the ones obtained by Fulle et al. (2015) who found a comparable decreasing trend of the rotational frequency during the pre-perihelion period. This trend lets us suppose that the majority of the particles lies on the very left part of the histogram, which can not be examined since the limited exposure time of our sample can only provide rotational frequencies above the minimum value of 0.24 Hz. Slower frequencies can be investigated looking at images with longer exposure time. Therefore, we expect that the particles do not rotate very fast in the inner coma, excluding a massive effect of fragmentation driven by their rotational motion. Overall, the tracks that show brightness variation are a percentage that range between 11-46% of the average number of tracks observed in a single image (see Table 3). Therefore, all tracks without brightness variation could be representative of either

very slow rotators, with periods larger than the exposure time of the image, or particles that are rotating exposing always the same face.

4.3 Flattening

The morphology of the dust of the order of hundreds of microns in 67P's coma was revealed by the images of the Micro-Imaging Dust Analysis System (MIDAS (Riedler et al. 2007)) and COSIMA (Mannel et al. 2016; Langevin et al. 2016). The dust particles show irregular shapes, they can be either fluffy aggregates or compact particles (Güttler et al. 2019). To give an estimate of their flattening, we evaluate the aspect ratio of particles via measurements of the maximum to minimum brightness ratio of the light curves, that represents the projected area of the aggregates on the plane of the image assuming uniaxial rotation and homogeneous composition. We decide to approximate these shapes with an ellipsoid of revolution, i.e. spheroid, which represents, as a first approximation, an irregular aggregate with two main cross sections on the plane of the image. Spheroids are also used as dust shape models by Fulle et al. (2015), Ivanovski et al. (2017a,b) Moreno et al. (2018) to represent the dynamics of the dust in the coma. The estimated aspect ratios are always larger than 1 (which is the value for a sphere), because we cannot discriminate between oblate and prolate spheroids. It means that a value equal to 2, for instance, could be attributed to a prolate spheroid but also to an oblate spheroid with aspect ratio 0.5. In Figure 13 the distribution of the aspect ratio values of the whole sample of particles is shown. The majority of the population lies between 1.1, for almost spherical particles, and 2. Nevertheless, the aspect ratio reaches values up to 11, revealing that the particles might be also very elongated (Fulle et al. 2017).

Following the results of Fulle et al. (2015) we might suppose a higher percentage of oblate spheroids rather than prolate. Ivanovski et al. (2017b) also found that oblate-like particles are the best candidates to reproduce GIADA data before perihelion. Muñoz et al. (2020) show that porous particles of an oblate-like shape oriented with its largest area facing the laser beam are necessary to reproduce the minimum of the OSIRIS phase functions at a phase angle of about 100 degrees, as observed by Bertini et al. (2017).

In Figure 14, we show the rotational frequency as a function of aspect ratio. The majority of the particles fill homogeneously an area defined by values of aspect ratio between 1 and 2 and with frequency between 0.24 and 0.56 Hz. Therefore, for those particles, it is not possible to infer a relation between rotational frequency and shape. Furthermore, we recognise two populations that deviate from the majority: one with high rotational frequency and low values of aspect ratio so more spherical particle, the other with high values of aspect ratio, up to about 11, which corresponds to very elongated particles with relatively slow rotational frequency. Indeed more elongated particles are expected to rotate slower than the spherical ones, and this is linked to their inertia momenta (Ivanovski et al. 2017b). So, if the majority of the population is composed by slow rotators we might expect more aggregates with high elongation.

5 PHOTOMETRY

In this section, we measure the photometry of the particles in the images taken in the period August 2015 - January 2016 (see Table 3). Then, we simulate the expected spectral radiances of the dust particles in the cometary coma with a scattering model. We compute the radiance of the single particles, changing a wide range of parameters such as the composition, size, heliocentric distance, and

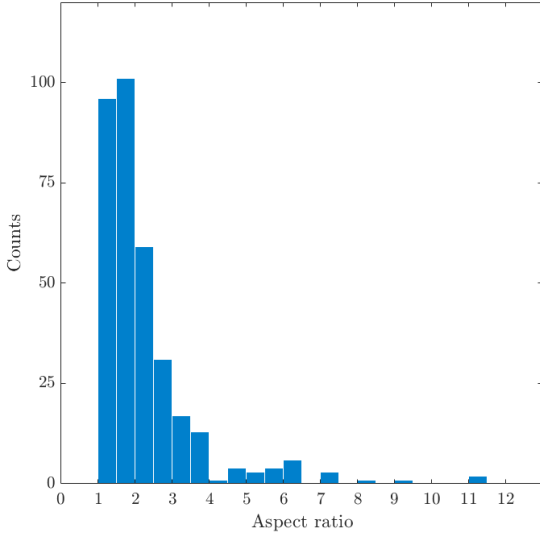


Figure 13. The histogram shows the ellipsoidal particles aspect ratio distribution listed in Table 3.

spacecraft distance. Finally, we compare them with the particles spectral radiances obtained directly from the images to estimate their size.

5.1 Scattering simulations

We use a scattering code in order to synthetically reproduce the photometry of the dust particles.

It takes into account a wide range of parameters such as the distance from the spacecraft and the Sun, the size of the particles, their phase angle, density and the type of material they are made of, evaluated through the refractive index.

The code computes the amount of light scattered by each dust particle towards the CCD by using the Mie theory for spherical particles (Wolf & Voshchinnikov 2004). The software is optimised to consider arbitrary large size parameters and to give a first estimate of the particles size. Input parameters of the code are the phase angle of the dust, the density, and the refractive index of the material. We fix the phase angle at 90 degrees and the density at 800 kg/m^3 (Fulle et al. 2016b). We select two characteristic compositions of the dust particles represented by the silicates, with refractive index $m = 1.6 + i10^{-5}$ (Muñoz et al. 2000; Frattin et al. 2019), and by the organics, with refractive index $m = 1.3 + i10^{-2}$ (Frattin et al. 2019). This choice is based on the observations of the 67P dust provided by the instruments on board the Rosetta s/c. COSIMA mass spectrometer has confirmed the presence of abundant high-molecular weight organic matter, nearly 50 % in mass (Bardyn et al. 2017; Fray et al. 2017). Half of the mass of each dust particle consists of carbonaceous material with a mainly macromolecular organic structure; the other half being mostly composed of non-hydrated silicate minerals. GIADA has found that the measured densities of the 67P pebbles are consistent with a mixture of $(15 \pm 6) \%$ of ices, $(5 \pm 2) \%$ of Fe-sulphides, $(28 \pm 5) \%$ of silicates, and $(52 \pm 12) \%$ of hydrocarbons, in average volume abundances (Fulle et al. 2016b, 2017). Frattin et al. (2017) have found hints on the presence of three major groups of dust particles, based on the analysis of their spectral slope between [535–882] nm obtained from OSIRIS images.

They found that the steepest spectra may be related with organic material, the spectra with an intermediate slope, can be a mixture of silicates and organics and the flat spectra may be associated with a high abundance of water ice (Frattin et al. 2017). Following these results, organics and silicates seem to be good representatives of the dust particles composition in the coma of 67P.

In Table B1 we report the expected spectral radiances for different combinations of the code parameters. We simulate particles with a size of 0.1, 1, 10 mm, at distance from the spacecraft that ranges from 1 km to 20 km, following the results shown in Figure 15. We fix the heliocentric distance at 1.3, 1.7 and 2.0 AU to best represent the observations. The resulting spectral radiances have values between 10^{-3} and $10^{-10} \text{ W/(m}^2 \text{ nm sr)}$. They are strongly dependent on the heliocentric distance, showing the highest values at perihelion and decreasing as the comet moves away from the Sun, and are brighter for silicate particles than for the organic ones.

5.2 Results

We perform the photometry of the rotating dust particles analysed in the previous section and reported in the dataset of Table 3. We evaluate the radiances of the whole track computing the sum of the signal of each pixel divided by the exposure time. In Figure 16 we see the distribution of the particle spectral radiances for each epoch. The values range between 10^{-6} and $10^{-3} \text{ W/(m}^2 \text{ nm sr)}$, but the large majority is between 10^{-5} and $10^{-4} \text{ W/(m}^2 \text{ nm sr)}$. The uncertainty associated to the radiometric calibration is less than 1% (Tubiana et al. 2015).

In order to give an estimate of the effective size (based on brightness) of the aggregates, we compared them with the simulated values. For the calibration, we use the data of Ott et al. (2017). We choose 2 aggregates at about 3–4 km from the spacecraft, at 1.25 AU from the Sun, with a cm-size as a reference (precisely number 8 and 9 of their Table 3). We find that the values of the spectral radiance, corrected for the phase function (Bertini et al. 2017), are respectively of $7.02 \pm 0.02 \cdot 10^{-4}$ and $5.15 \pm 0.02 \cdot 10^{-4} \text{ W/(m}^2 \text{ nm sr)}$, where the uncertainty is the standard deviation of the background. These results are strongly compatible with the simulations, whether we consider either organics or silicates. As a result, we find that the most populated values of spectral radiance correspond to mm and cm-size. The faintest value of radiance might be compatible with a particle size of the order of 0.1 mm (if very close to the s/c, i.e. 1 km) in both the cases of silicates and organics. Simulated particles smaller than mm have spectral radiances fainter than $10^{-7} \text{ W/(m}^2 \text{ nm sr)}$, a value that is outside the range obtained in the observations. Therefore, our analysis of rotational particles suggests that the majority of the dust aggregates we observe might likely have sizes that range from mm to cm.

5.3 Particles Distance and Size

We estimate the minimum size of the observed rotating particles, based on the radiance computed with the scattering model. The faintest measured spectral radiance has value equal to $3 \cdot 10^{-6} \text{ W/(m}^2 \text{ nm sr)}$. We use the results of the scattering model to determine the minimum possible size corresponding to this radiance. To do this we set the heliocentric distance and the spacecraft distance of the particles at their minimum values, respectively $r_h = 1.3 \text{ AU}$ and $d_{s/c} = 1 \text{ km}$. In fact, the smaller is the distance of the particles from the Sun and from the spacecraft and the higher is their radiance. In this way, the possibility to detect a small particle is maximised. We see

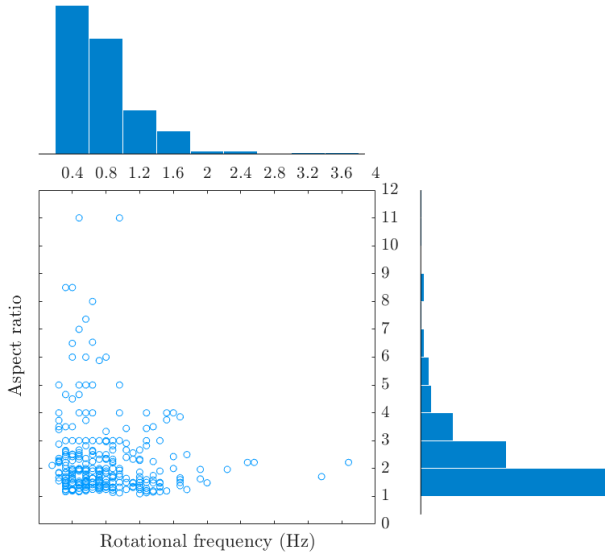


Figure 14. The figure shows the distribution of the particles in the parameter space defined by the particle aspect ratios and the rotational frequencies with their respective histograms.

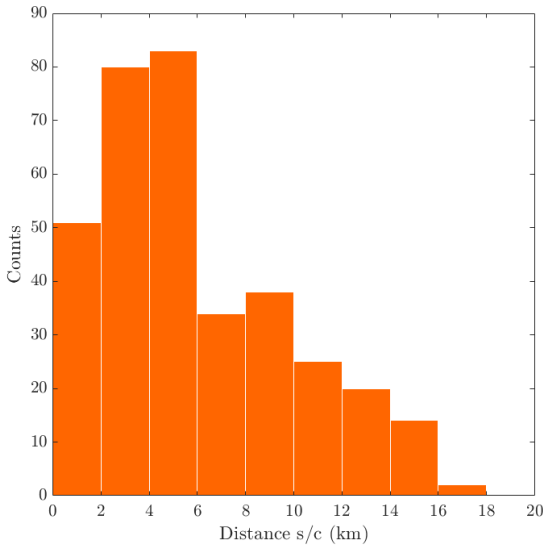


Figure 15. In the figure the distribution of the particle estimated distances from the spacecraft is shown.

that the radiance equal to $3 \cdot 10^{-6}$ matches to a particle smaller than 1 mm (to which corresponds a radiance equal to $3 \cdot 10^{-5}$) but larger than 0.1 mm (to which corresponds a radiance equal to $3 \cdot 10^{-7}$). Therefore, the particles that we observe in this work are at least of the order of 0.5 mm. This is a lower limit computed in case of particular conditions therefore we expect the majority of the particles to be larger than that limit. The same size range was studied by Ott et al. (2017) who found particles from $1.5 \cdot 10^{-3}$ m up to 0.32 m with an average value of 0.05 m. They were able to measure also the speed of those particles, finding that the 90% of them had values between 0 - 5 m/s with statistic mode equal to 1.25 m/s (see their Figure 9). The detection of rotating particles is affected by a

bias that facilitates the observation of larger and slower particles. Indeed, very small and faint particles should approach the spacecraft very close to be detected and consequently they would move out of focus. Moreover, particles of the order of 0.1 mm or even smaller, as those measured by GIADA (Rotundi et al. 2015; Della Corte et al. 2015) might reach high velocity and the tracks they generate extend along more pixels with a consequent decrease of intensity that complicates the detection. Therefore, based on the scattering model and on the previous assumptions, we have reasons to think that the tracks observed in these set of images are generated by particles likely larger than 1 mm. Furthermore, the track signal must be high to be able to reveal a brightness variation, thus excluding the fainter particles from the sample. Following this assumption, we use the velocity found by Ott et al. (2017) for particles in the same range of size. We approximate the average velocity at which the observed particles move inside the coma with their statistic mode, $v = 1.25$ m/s. Moreover, we suppose that within the same image the longest tracks represent on average closer particles, while the shorter ones are particles far away from the spacecraft.

The length and the number of rotations depend also on the mass and the size of the particles. We expect that the smallest and lowest density particles reach higher velocity and angular velocity than the large and dense ones (Ivanovski et al. 2017a). In the latter paper, the authors show that this could change if large particles of low density and small particles of high density are studied. In Section 6 we show the results of dust modeling of particles with the same derived dynamical characteristics obtained by this analysis of the observed light curves. Nevertheless, a first investigation can be done, to provide hints about those rotating particles.

We use the length of the tracks to measure the distance of the single particles. In the approximation that the particle velocity distribution mode is a good indicator of the average speed of the observed particles, it is straightforward that the average length covered by a dust particle in 12.5 seconds of exposure time is of $v \cdot t = 15.625$ m. Therefore, it is possible to construct the following spatial scale: $v \cdot t / l = 15.625 / l$ m/px, where l is the length of the tracks in pixel. On the other side, the spatial scale of the NAC camera is 1.86 m/px at 100 km from the spacecraft. Equalling the two scales leads to the following expression:

$$1.86 : 100 = \frac{v \cdot t}{l} : d_{s/c} \quad (4)$$

from which $d_{s/c}$, the distance of the particles from the spacecraft is immediately computed. The results are shown in Figure 15, where the histogram represents the average distance distribution. Eventually, the particles analysed in this work, which are observed with the Orange filter at $\lambda = 649$ nm, with an exposure time of 12.5 seconds seem to reach distance from the spacecraft of less than 20 km.

Ultimately, we compute the size of the rotating particles. We compare the observed values of the spectral radiance of each dust particle with the values obtained with the scattering model at proper heliocentric and spacecraft distances, reported in Appendix B. Each combination of these three parameters (r_h , $d_{s/c}$ and the radiance) corresponds to a specific size. In Figure 17 we show the parameter space composed by the observed spectral radiances and distances of the dust population listed in Table 3. The distribution of the particles along the line of sight size is shown in Figure 18. The cm-sized group seems to be the most populated. These results are consistent with the direct measurements of Ott et al. (2017), that found that the bulk of particles has sizes of centimetres.

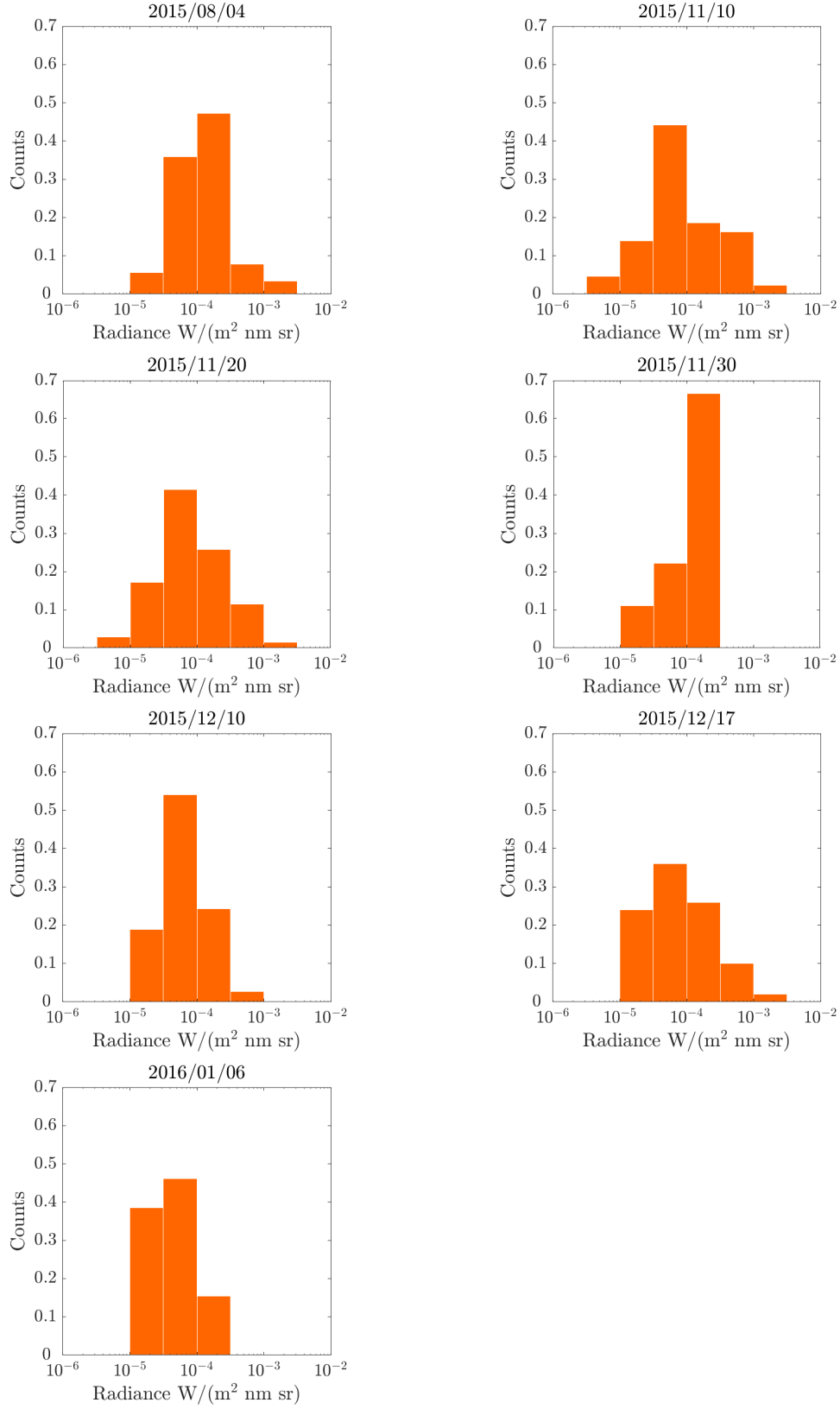
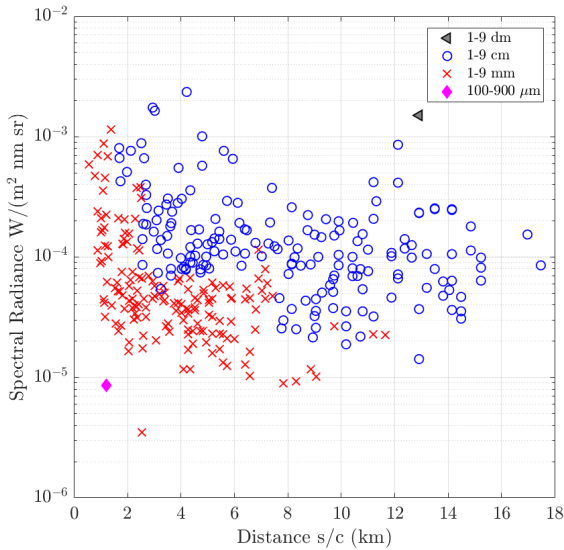
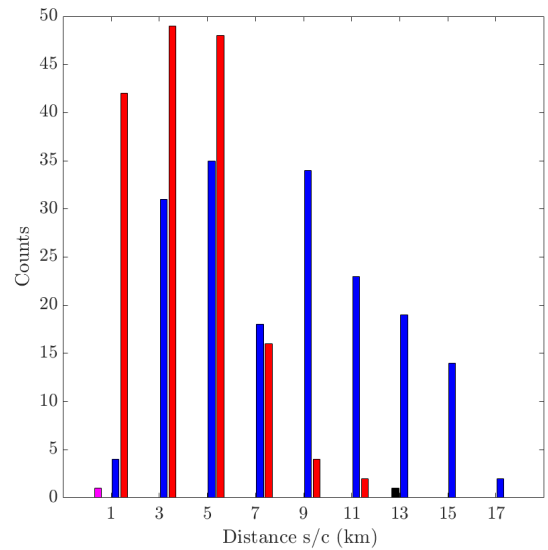


Figure 16. The graphics show the histograms of the dust particle spectral radiances for each epoch from the data set illustrated in Table 3. The sample consists in the same rotating particles analysed in Section 4. The counts are normalised to 1. The spectral radiance is corrected for the phase function and it is in units of $W/(m^2 \text{ nm sr})$.

Input parameter	Parameter value	Comments
Particle parameters		
Particle size [m]	$1.0 \times 10^{-3} - 1.0 \times 10^{-1}$	Observational constraint derived from this study
Particle density [kg/m ³]	800	Constrained by the GIADA data (Fulle et al. 2016a, 2017)
Spheroid aspect ratio, a/b	2/3 and 3/2	Observational constrain derived as the most relevant in this study
Initial particle orientation [deg]	$22.5 - 67.5^\circ$	Compatible with the one used to reproduce particle speeds measured by GIADA (Ivanovski et al. 2017b)
Particle temperature, T_d [K]:	300	Fulle et al. (2020)
67P/CG parameters		
Radius, R_N [m]	2.0×10^3	Sierks et al. (2015)
Mass, m_N [kg]	1.0×10^{13}	Pätzold et al. (2016)
Total gas production [mol/s]	10^{28}	Hansen et al. (2016)

Table 1. The dust model initial parameters used in this work.**Figure 17.** The plot illustrates the distribution of the dust particles in the parameter space defined by their spectral radiances and estimated distances from the spacecraft. The black triangle is a dm-sized particle, the blue circles are the cm-sized particles, the red crosses are the mm-sized particles while the magenta diamond is a μ m-sized particle.**Figure 18.** The histogram represents the distribution of the dust particles of different size along the line of sight. The black bars represent the dm-sized particles, the blue ones the cm-sized particles while the red ones the mm-sized particles.

6 DUST DYNAMICAL SIMULATIONS OF ROTATING NON-SPHERICAL PARTICLES

The 3D+t non-spherical cometary dust model (Fulle et al. 2015; Ivanovski et al. 2017a,b) has been the first one applied to Rosetta data and allowed to obtain those dust physical parameters that were not possible to measure by the on-board instruments due to the operational limitations or instrumental design. First, the model was used in Fulle et al. (2015) to interpret the brightness variation of the tracks in OSIRIS images taken in October 2014. In the present work, we apply the model to datasets of NAC images from July 2015 to January 2016 considering the physical conditions present in 67P coma during this period. We compute the particle rotational frequencies and terminal velocities. We provide a plausible scenario for interpreting the data assuming initial parameters that can lead to the rotational frequencies derived from the observations.

6.1 Model and setup

We consider homogeneous spheroids with aspect ratio 1.5 - the most probable obtained by the observations in this study. The two main forces acting on the dust particles in closer vicinity to the nucleus are the aerodynamic force and gravity. The analysis of the images show mainly radial outflow (Section 3). We consider that the gas approximation for calculating the aerodynamic force is the Euler one for an expanding ideal gas (Landau & Lifshitz 1987), which is less time and computationally consuming. The calibration of the physical parameters of these gas solutions is obtained using the GIADA data and the gas production rates reported in Hansen et al. (2016). We shortly review the equations governing the motion

of given dust particle:

$$m_d \frac{d^2 \vec{r}}{dt^2} = m_d \frac{d\vec{V}_d}{dt} = \vec{F}_N + \vec{F}_a$$

$$\vec{F}_N = -G \frac{m_N m_d}{r^3} \vec{r} \quad (5)$$

$$\vec{F}_a = - \int \left(p \vec{n} + \tau \left[(\vec{V}_r \times \vec{n}) \times \vec{n} \right] / |\vec{V}_r \times \vec{n}| \right) ds,$$

where \vec{r} and \vec{V}_d are the radius-vector and the velocity of the center of mass of the particle in the cometocentric non rotating frame x, y, z ; m_d is the particle mass; m_N is the nucleus mass, \vec{V}_r is the gas velocity relative to the elementary surface element of the particle, and \vec{F}_N and \vec{F}_a are the gravity and the aerodynamic forces; p, τ are the gas pressure and the shear stress on the elementary surface element of the particle with area ds (for the exact free molecular expressions, see Shen (2006)); \vec{n} is the outward unit vector normal to the elementary surface element, and G is the gravitational constant. Since the minimal collisional mean free path of the gas molecules on the surface is of the order of tens of metres, i.e. much bigger than the considered particle sizes, the flow over the particles may be considered as free molecular (Ivanovski et al. 2017a).

We integrate equations (5) and the Euler dynamical and kinematic equations (Landau & Lifshitz 1969, for details) for large distances (Ivanovski et al. 2017b). The gravitational, \vec{M}_N , and aerodynamic, \vec{M}_a , torques necessary for computing the Euler dynamical equations are given by:

$$\vec{M}_N = - \int G m_N \vec{\rho} \frac{\vec{l}_s \times \vec{r}}{r^3} d\Gamma$$

$$\vec{M}_a = - \int \vec{l}_s \times \left(p \vec{n} + \tau \left[(\vec{V}_r \times \vec{n}) \times \vec{n} \right] / |\vec{V}_r \times \vec{n}| \right) ds \quad (6)$$

where $d\Gamma$ is the elementary volume of the particle, \vec{l}_s is the radius-vector towards ds or $d\Gamma$ from the center of mass of the particle, and $\vec{\rho}$ is the dust specific mass.

For the goals of this study, we use the dust parameters constrained by the observations in this paper and the physical parameters of 67P as its mass, gas production and surface temperature in the considered period. Table 1 summarises the simulation parameters in two different sets. The first set includes the physical properties of the simulated particles. The second set reviews the 67P measured physical parameters used for the gravity force computation. In particular, we assume a particle bulk density of 800 kg m^{-3} (Fulle et al. 2017) and non zero initial velocity (see the next subsection). We assume that the particles do not contain any volatiles nor do they fragment, i.e. keep their shape and mass during the whole motion.

6.2 Computed rotational frequencies and particle speeds

We compute the velocities of spheroidal particles with different aspect ratio $a/b = 2/3$ and $3/2$ (oblate and prolate) ranging from $b = 0.01$ to 1 m . Figure 19 shows the computed particle velocities and rotational frequencies of spheroids of the same size ($b = 1 \text{ cm}$) and density (800 kg m^{-3}) as found as the most probable candidates derived in the present study from the analysis of the OSIRIS data. These velocities and rotation frequencies are close to those in Ivanovski et al. (2017b) found for particles of the same size, moving in the same gas field, but with density 1000 kg m^{-3} and $a/b = 2.0$. In the present simulations the gas production rate is 100 times greater than used in Fulle et al. (2015) (due to the variation of the gas production from pre-landing period in October 2014 to perihelion in August 2015). The results show that the considered particles remain slow rotators ($< 0.01 \text{ Hz}$).

Figure 12 shows that the majority of the observed particles have frequency $\sim 0.4 \text{ Hz}$. The most brightness frequency in October 2014 data was 0.3 Hz , while during and post perihelion is 0.4 Hz . If we compute the most probably rotational frequency considering both the shorter exposure time 12.5 s ($\sim 2/3$ of the one used in the measurements during 12-13 and 19-20 October 2014 (Figure 4, Fulle et al. (2015))) and the most probable frequency of those periods i.e. ~ 0.3 , we obtain as a most probable frequency ~ 0.4 i.e. the same as the one derived in our measurements analysis. The latter fact evidences that the most probable rotational frequency has not changed when approaching the Sun.

Since the perihelion data analysis can not disentangle the prolate of oblate shapes, we perform simulations for both shapes, i.e. $a/b = 2/3$ and $3/2$. The oblate particle obtain higher rotational frequency than the prolate particle, but it is still lower than derived from the observations. Among the possible explanations could be uncertainty of the particle detachment process (i. e. presence of initial velocity and/or torque and/or rocket force due to particle sublimation). Therefore we perform simulations for these spheroids assuming that they have initial velocity which corresponds to the maximum possible ejection velocity of a particle with the same volume and mass estimated for 67P nucleus in Fulle et al. (2020) (assuming complete transfer of the gas thermal energy at the detachment into the initial kinetic energy of the particle). This initial velocity is of few centimetres per second and does not affect the resulting rotational motion in our simulations. Owing to the large uncertainty in the values to be adopted for the initial torque and possible outgasing from the particle we do not try to address this in the current work. A preliminary study shows that the high initial rotational frequencies ($> 0.4 \text{ Hz}$) can remain unchanged during the particle motion through the coma.

7 SUMMARY AND CONCLUSIONS

In this work, we have analysed a collection of images of the inner coma of the comet 67P/Churyumov-Gerasimenko with the aim of describing the physical and dynamical properties of the single dust particles to provide constraints for theoretical 3D coma models.

In Section 3 we performed a dynamical analysis of the particles in the inner coma of 67P. We measured the direction of motion directly from the images revealing highly radial trajectories with respect to the nucleus. This suggested that the material originated from the nucleus and that all deviations from the radially might be interpreted as a small population of bound orbiting objects.

In Section 4 we focused on a group of particles that showed evidence of rotational motion. The sample represented about the 18% of the whole population, while the remaining showed homogeneously bright tracks. We measured a rotational frequency with a decreasing trend up to a maximum value of $\nu = 3.6 \pm 0.2 \text{ Hz}$. It was not possible to detect particles with values of rotational frequency below 0.24 Hz since the exposure time of the images was not long enough to identify slow rotating objects. The decreasing trend of the frequency distribution and the fact that the sample represented only a small part of the overall dust particles population suggested that the majority of them rotated slower than the group studied in this work. Consequently, no fragmentation of the aggregates was expected. The light curves analysis provided also the aspect ratio of the single dust particles in the approximation of ellipsoidal shape, contributing to characterise them. The majority of the population had values that range between 1 and 2, revealing a moderate level of flattening. Nevertheless, the aspect ratio reached values quite

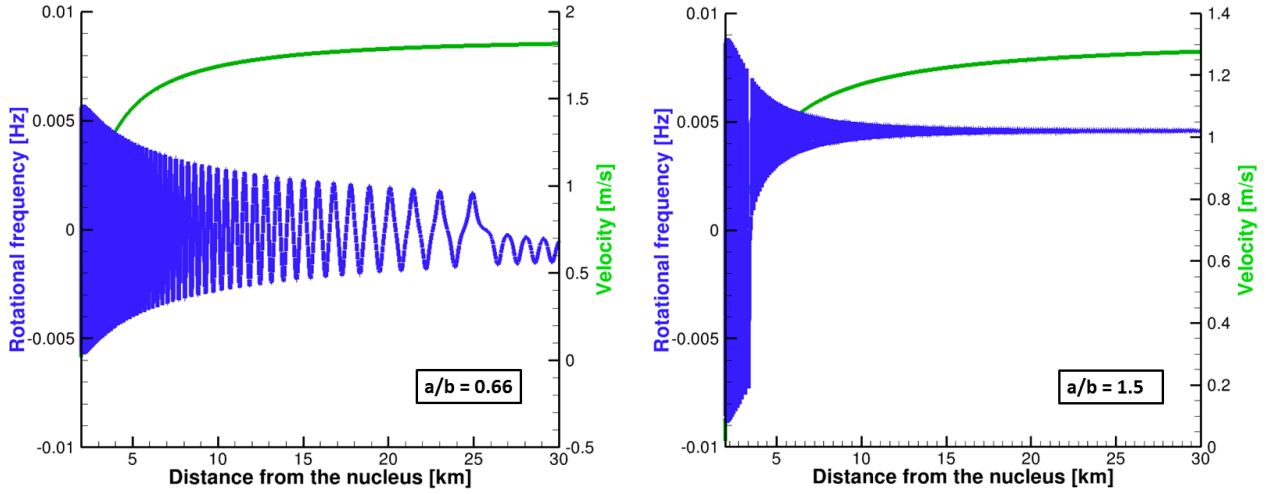


Figure 19. Particle velocity (green lines) and rotational frequencies (blue lines) in two cases: spheroid with aspect ratio $a/b = 0.66$ (left) and spheroid with aspect ratio $a/b = 1.5$ (right). Both spheroids are with size $b = 1$ cm in radius and bulk density 800 kg/m^{-3} is considered. The complete list of the particle parameters are given in Table 1.

high, up to 11, revealing the particles might be also very elongated. In Section 5 we performed the photometric analysis of the same samples of particles used in the previous section. We measured their fluxes and, by comparing them with simulated ones we derived their size. We took into account two types of composition, i.e. silicates and organic, and we computed the radiance produced by different sizes at different distances from the camera with a Mie scattering model. The direct comparison of the simulated fluxes with the observed ones provided a size distribution of the particles that ranged from the value of millimetres up to the decimetres. Following those calculations, it seemed that the camera was not able to detect particles smaller than millimetres (except one case of a particle of the order of 0.1 mm) since they should have had a flux fainter than the background.

These observational measurements worked as constraints for the theoretical dynamical model used in Section 6 to compute the velocity and rotational frequencies of the dust particles. The results of the simulation showed that particles with the same characteristics of the observed ones remained slow rotators ($\nu < 0.01$ Hz). Therefore, the simulations confirmed that the majority of the particle population should have had a low rotational frequency. The explanation to characterise the motion of the fast rotating particles still misses. A possible hint could be related with the uncertainty of the particle detachment processes that might transmit them an initial rotational velocity.

Data Availability All the data underlying this paper are available at <https://www.cosmos.esa.int/web/psa/rosetta>.

REFERENCES

- Acton C. H., 1996, *Planet. Space Sci.*, **44**, 65
- Bardyn A., et al., 2017, *MNRAS*, **469**, S712
- Bertini I., et al., 2017, *MNRAS*, **469**, S404
- Bertini I., et al., 2019, *MNRAS*, **482**, 2924
- Colangeli L., et al., 2007, *Space Sci. Rev.*, **128**, 803
- Crifo J. F., Loukianov G. A., Rodionov A. V., Khanlarov G. O., Zakharov V. V., 2002, *Icarus*, **156**, 249
- Crifo J.-F., Loukianov G. A., Rodionov A. V., Zakharov V. V., 2005, *Icarus*, **176**, 192
- Della Corte V., et al., 2014, *Journal of Astronomical Instrumentation*, **3**, 1350011
- Della Corte V., et al., 2015, *A&A*, **583**, A13
- Della Corte V., et al., 2016, *MNRAS*, **462**, S210
- Frattin E., et al., 2017, *MNRAS*, **469**, S195
- Frattin E., et al., 2019, *MNRAS*, **484**, 2198
- Fray N., et al., 2017, *MNRAS*, **469**, S506
- Fulle M., Blum J., 2017, *MNRAS*, **469**, S39
- Fulle M., et al., 2015, *A&A*, **583**, A14
- Fulle M., et al., 2016a, *MNRAS*, **462**, S132
- Fulle M., et al., 2016b, *ApJ*, **821**, 19
- Fulle M., et al., 2017, *MNRAS*, **469**, S45
- Fulle M., Blum J., Rotundi A., Gundlach B., Güttler C., Zakharov V., 2020, *MNRAS*, **493**, 4039
- Güttler C., et al., 2019, *A&A*, **630**, A24
- Hansen K. C., et al., 2016, *MNRAS*, **462**, S491
- Ivanovski S. L., Zakharov V. V., Della Corte V., Crifo J.-F., Rotundi A., Fulle M., 2017a, *Icarus*, **282**, 333
- Ivanovski S. L., et al., 2017b, *MNRAS*, **469**, S774
- Keller H. U., et al., 2007, *Space Sci. Rev.*, **128**, 433
- Landau L. D., Lifshitz E. M., 1969, *Mechanics*
- Landau L. D., Lifshitz E. M., 1987, *Fluid Mechanics*
- Langevin Y., et al., 2016, *Icarus*, **271**, 76
- Le Roy L., Bardyn A., Briois C., Cottin H., Fray N., Thirkell L., Hilchenbach M., 2015, *Planet. Space Sci.*, **105**, 1
- Mannel T., Bentley M. S., Schmied R., Jeszenszky H., Levasseur-Regourd A. C., Romstedt J., Torkar K., 2016, *MNRAS*, **462**, S304
- Marschall R., et al., 2016, *A&A*, **589**, A90
- Moreno F., et al., 2017, *MNRAS*, **469**, S186
- Moreno F., et al., 2018, *AJ*, **156**, 237
- Muñoz O., Volten H., de Haan J. F., Vassen W., Hovenier J. W., 2000, *A&A*, **360**, 777
- Muñoz O., et al., 2020, *ApJS*, **247**, 19
- Ott T., et al., 2017, *MNRAS*, **469**, S276
- Pätzold M., et al., 2016, *Nature*, **530**, 63
- Riedler W., et al., 2007, *Space Sci. Rev.*, **128**, 869
- Rotundi A., Ferrini G., Baratta G. A., Palumbo M. E., Palomba E., Colangeli L., 2007, *Dust in Planetary Systems*, **643**, 149
- Rotundi A., et al., 2008, *Meteoritics and Planetary Science*, **43**, 367
- Rotundi A., et al., 2015, *Science*, **347**, aaa3905

- Shen C., 2006, *Rarefied Gas Dynamics: Fundamentals, Simulations and Micro Flows*. Heat and Mass Transfer, Springer Berlin Heidelberg, <https://books.google.it/books?id=GdJpYCwMDROC>
- Sierks H., et al., 2015, *Science*, **347**, aaa1044
- Skorov Y., Reshetnyk V., Lacerda P., Hartogh P., Blum J., 2016, *MNRAS*, **461**, 3410
- Skorov Y., Reshetnyk V., Rezac L., Zhao Y., Marschall R., Blum J., Hartogh P., 2018, *MNRAS*, **477**, 4896
- Tubiana C., et al., 2015, *A&A*, **583**, A46
- Wolf S., Voshchinnikov N. V., 2004, *Computer Physics Communications*, **162**, 113
- Zakharov V. V., Rodionov A. V., Lukianov G. A., Crifo J. F., 2009, *Icarus*, **201**, 358
- Zakharov V. V., Ivanovski S. L., Crifo J. F., Della Corte V., Rotundi A., Fulle M., 2018, *Icarus*, **312**, 121

ACKNOWLEDGEMENTS

OSIRIS was built by a consortium of the Max-Planck-Institut für Sonnensystemforschung in Göttingen, Germany; CISAS-University of Padova, Italy; the Laboratoire d'Astrophysique de Marseille, France; the Instituto de Astrofísica de Andalucía, CSIC, Granada, Spain; the Research and Scientific Support Department of the European Space Agency, Noordwijk, The Netherlands; the Instituto Nacional de Técnica Aeroespacial, Madrid, Spain; the Universidad Politécnica de Madrid, Spain; the Department of Physics and Astronomy of Uppsala University, Sweden; and the Institut für Datentechnik und Kommunikationsnetze der Technischen Universität Braunschweig, Germany. The support of the national funding agencies of Germany (DLR), Italy (ASI), France (CNES), Spain (MEC), Sweden (SNSB), and the ESA Technical Directorate is gratefully acknowledged.

GIADA was built by a consortium led by the Univ. Napoli Parthenope INAF- Oss. Astr. Capodimonte, in collaboration with the Inst. de Astrofísica de Andalucía, Selex-ES, FI and SENER. GIADA was managed and operated at INAF-IAPS. GIADA was funded and managed by the Agenzia Spaziale Italiana, IT, with the support of the Spanish Ministry of Education and Science MEC, ES.

We thank the ESA teams at ESAC, ESOC, and ESTEC for their work in support of the Rosetta mission.

This research has been supported by the Italian Space Agency (ASI) within the ASI-INAF agreements I/032/05/0, I/024/12/0 and ASI 2020-4-HH.0.

Fernando Moreno acknowledges financial support from the Spanish Plan Nacional de Astronomía y Astrofísica LEONIDAS project RTI2018-095330-B-I00, project P18-RT-1854 from Junta de Andalucía, and the Centro de Excelencia Severo Ochoa Program under grant SEV-2017-0709.

Elisa Frattin acknowledges funding from Italian Ministry of Education, University and Research (MIUR) through the "Dipartimenti di eccellenza" project Science of the Universe.

MTP	STP	Activity	Epoch	Start time	Δt (hh mm ss)	r_c (km)	r_h (AU)	α ($^\circ$)	ϵ ($^\circ$)
021	075	GRAIN_COLOR_002	2015.09.28	14:42:32.150	01:04.00	1220	1.37	50	90-160
021	078	GRAIN_COLOR_004	2015.10.18	02:51:30.857	01:28.00	437	1.47	65	70-150
022	079	GRAIN_COLOR_001	2015.10.23	20:04:28.191	01:28.00	389	1.51	63	70-130
022	081	GRAIN_COLOR_002	2015.11.06	20:05:59.163	01:31.00	244	1.61	63	55-140
023	083	GRAIN_COLOR_001	2015.11.19	13:11:24.629	01:36.00	126	1.70	74	50-130

Table 2. OSIRIS data set used in Section 3 to measure the particles direction of motion and their alignment with nucleus and Sun directions. MTP: medium time planning of the dataset. STP: short time planning of the dataset. Activity: the activity name of the sequence. Epoch: image acquisition day. Start time: image initial acquisition time. Δt : range of time between the first and last image acquisition. r_c : nucleocentric distance. r_h : heliocentric distance. α : phase angle as shown in Figure 1 (i.e. angle between spacecraft and Sun as seen by the comet). ϵ : elongation of the Sun (i.e. angle between the camera pointing direction and the Sun as seen by the s/c). The exposure time of each image is 12.5 s.

MTP	STP	Activity	Epoch	Start time	Δt (hh mm ss)	r_c (km)	r_h (AU)	α ($^\circ$)	ϵ ($^\circ$)	γ ($^\circ$)	#rot	#im	#tot	%rot	f (Hz)	a/b	bkg
019	067	GRAIN_COLOR_002	2015.08.04	14:20:31.208	01:15.19	238	1.25	90	135	45	89	8	599	25	0.4	1.5	$3 \cdot 10^{-7}$
022	081	GRAIN_TRACK_003	2015.11.10	13:32:44.361	03:30.01	202	1.61	62	137	19	43	12	284	22	0.4	1.5	$2 \cdot 10^{-7}$
023	083	GRAIN_TRACK_001	2015.11.20	18:29:26.800	03:20.01	142	1.70	87	122	29	70	6	355	30	0.4	1.9	$2 \cdot 10^{-7}$
023	084	GRAIN_TRACK_002	2015.11.30	17:56:25.051	02:20.01	111	1.70	90	120	30	9	7	107	11	0.4	1.1	$1 \cdot 10^{-7}$
023	086	GRAIN_TRACK_003	2015.12.10	17:32:23.417	03:50.00	99	1.86	89	76	-15	74	10	301	41	0.8	2.4	$4 \cdot 10^{-7}$
024	087	GRAIN_TRACK_001	2015.12.17	01:53:01.775	04:30.00	100	1.9	90	106	16	50	12	198	46	0.4	1.3	$1 \cdot 10^{-7}$
024	090	GRAIN_TRACK_003	2016.01.06	11:13:43.828	02:40.00	84	2.06	90	75	-15	13	9	72	38	1.6	1.6	$2 \cdot 10^{-7}$

Table 3. OSIRIS data set used in Section 4 for the analysis of dust rotational motion. MTP: medium time planning of data acquisition. STP: short time planning of data acquisition. Activity: the activity name of the sequence. Epoch: image acquisition day. Start time: image initial acquisition time. Δt : range of time between the first and last image acquisition. r_c : nucleocentric distance. r_h : heliocentric distance. α : phase angle as shown in Figure 2. ϵ : elongation of the Sun (i.e. angle between the camera pointing direction and the Sun as seen by the s/c). γ : angle between the comet and the pointing direction as seen by the s/c. #rot: number of rotating particles individuated in each dataset. #im: number of images analysed for each dataset. #tot: total number of particles in the dataset. %rot: percentage of rotating particles with respect to the total. f : average mode of the rotating frequency. a/b: average aspect ratio of the particles as defined in Section 4.3. bkg: value of the background averaged over each dataset in $W/(m^2 mm sr)$, computed on an area of 30 pixel radius of each image. Since the illumination condition is fixed the background variation among each dataset is negligible. The exposure time of each image is 12.5 s.

APPENDIX A: TRANSLATIONAL MOTION OF THE DUST

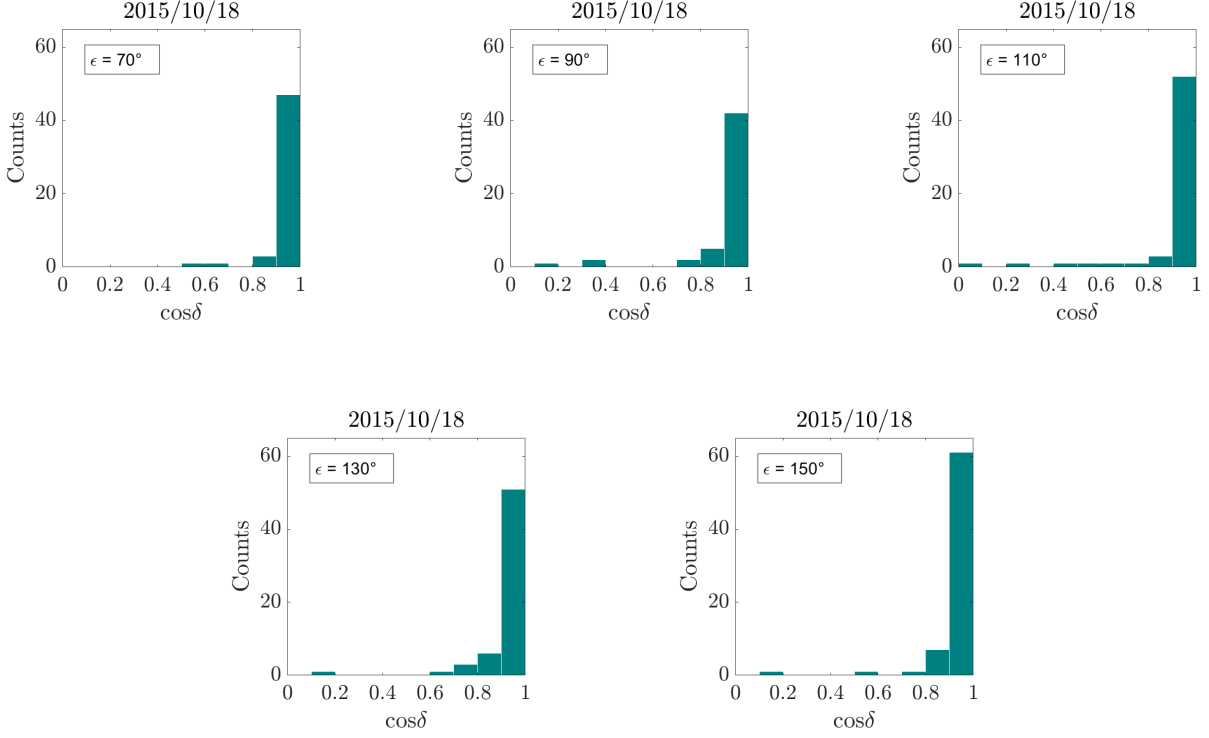


Figure A1: The histograms show the value of the cosine of the angle δ between the velocity vector of the particle on the image plane, and the projected position vector of the nucleus on the plane of the image, in the NAC reference system, for the set STP 078 GRAIN_COLOR_004.

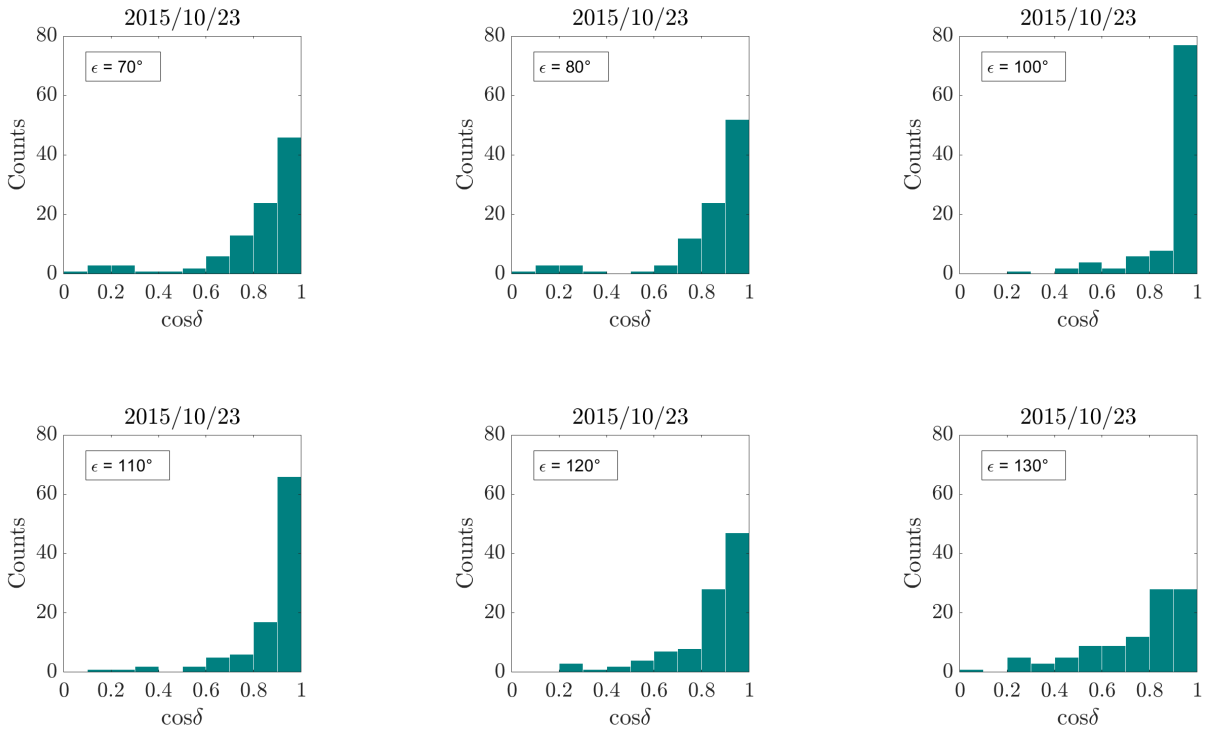
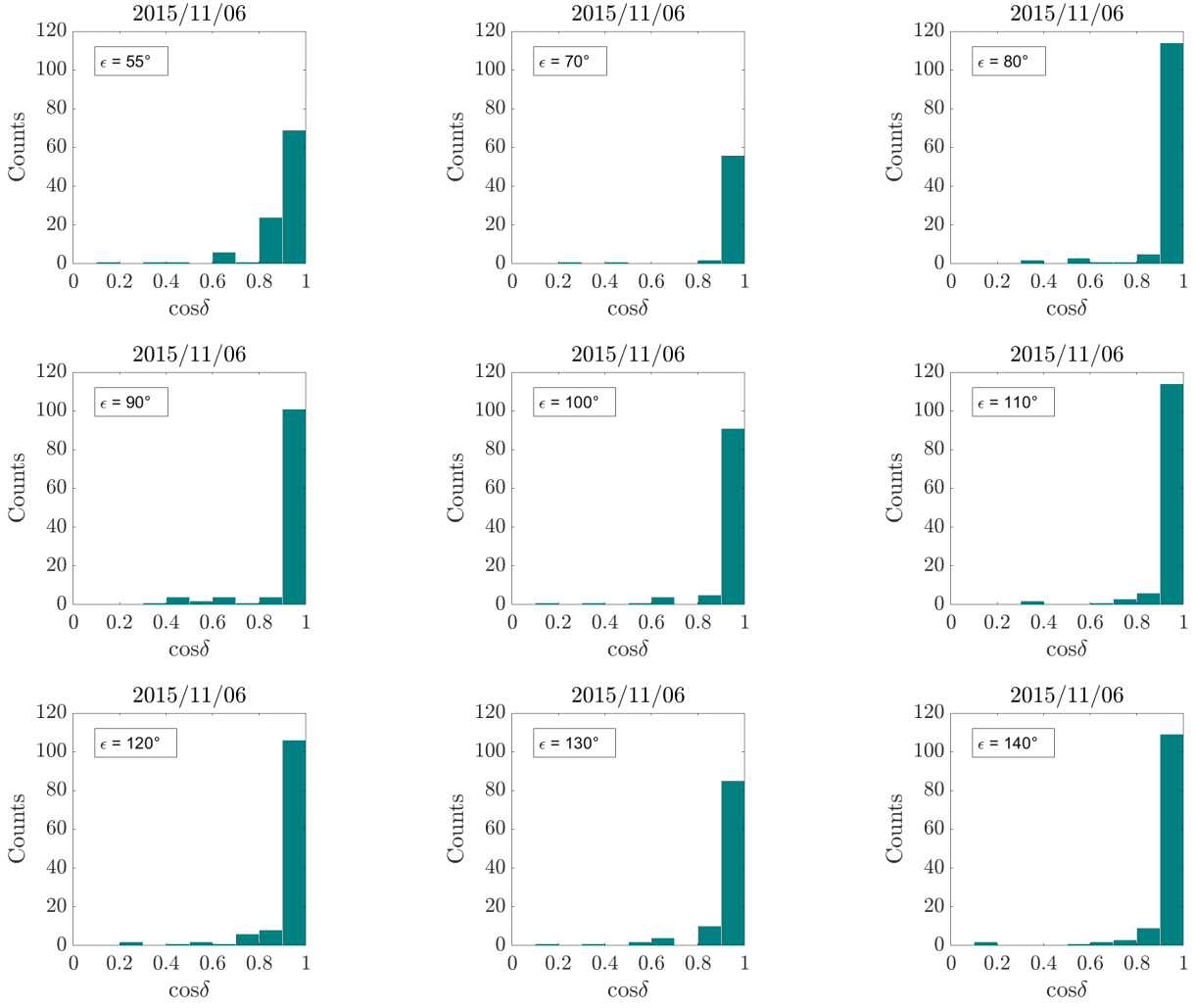
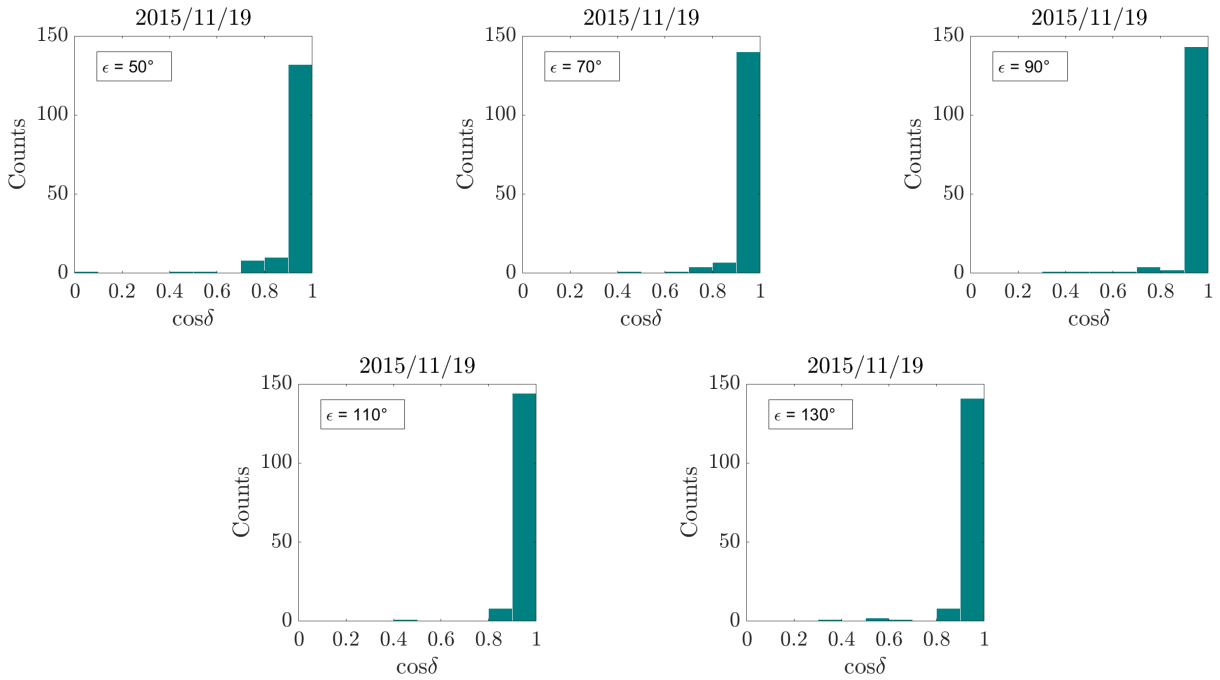


Figure A2: The histograms show the value of the cosine of the angle δ for the set STP 079 GRAIN_COLOR_001.

Figure A3: The histograms show the value of the cosine of the angle δ for the set STP 081 GRAIN_COLOR_002.Figure A4: The histograms show the value of the cosine of the angle δ for the set STP 083 GRAIN_COLOR_001.

APPENDIX B: SCATTERING SIMULATIONS

r_h (AU)	a (mm)	$d_{s/c}$ (km)	Silicates Radiance	Organics Radiance
1.3	0.1	1	$8.2 \cdot 10^{-7}$	$3.0 \cdot 10^{-7}$
		2	$2.1 \cdot 10^{-7}$	$7.5 \cdot 10^{-8}$
		5	$3.3 \cdot 10^{-8}$	$1.2 \cdot 10^{-8}$
		10	$8.2 \cdot 10^{-9}$	$3.0 \cdot 10^{-9}$
		15	$3.7 \cdot 10^{-9}$	$1.3 \cdot 10^{-9}$
		20	$2.1 \cdot 10^{-9}$	$7.5 \cdot 10^{-9}$
1.3	1	1	$1.0 \cdot 10^{-4}$	$3.0 \cdot 10^{-5}$
		2	$2.5 \cdot 10^{-5}$	$7.5 \cdot 10^{-6}$
		5	$4.0 \cdot 10^{-6}$	$1.2 \cdot 10^{-6}$
		10	$1.0 \cdot 10^{-6}$	$3.0 \cdot 10^{-7}$
		15	$4.4 \cdot 10^{-7}$	$1.3 \cdot 10^{-7}$
		20	$2.5 \cdot 10^{-7}$	$7.5 \cdot 10^{-8}$
1.3	10	1	$7.6 \cdot 10^{-3}$	$2.9 \cdot 10^{-3}$
		2	$1.9 \cdot 10^{-3}$	$7.3 \cdot 10^{-4}$
		5	$3.0 \cdot 10^{-4}$	$1.2 \cdot 10^{-4}$
		10	$7.6 \cdot 10^{-5}$	$2.9 \cdot 10^{-5}$
		15	$3.4 \cdot 10^{-5}$	$1.3 \cdot 10^{-5}$
		20	$1.9 \cdot 10^{-5}$	$7.3 \cdot 10^{-6}$
1.7	0.1	1	$4.8 \cdot 10^{-7}$	$1.8 \cdot 10^{-7}$
		2	$1.2 \cdot 10^{-7}$	$4.5 \cdot 10^{-8}$
		5	$1.9 \cdot 10^{-8}$	$7.2 \cdot 10^{-9}$
		10	$4.8 \cdot 10^{-9}$	$1.8 \cdot 10^{-9}$
		15	$2.1 \cdot 10^{-9}$	$8.0 \cdot 10^{-10}$
		20	$1.2 \cdot 10^{-9}$	$4.5 \cdot 10^{-10}$
1.7	1	1	$5.8 \cdot 10^{-4}$	$1.8 \cdot 10^{-5}$
		2	$1.5 \cdot 10^{-5}$	$4.5 \cdot 10^{-6}$
		5	$2.3 \cdot 10^{-6}$	$7.2 \cdot 10^{-7}$
		10	$5.8 \cdot 10^{-7}$	$1.8 \cdot 10^{-7}$
		15	$2.6 \cdot 10^{-7}$	$8.0 \cdot 10^{-8}$
		20	$1.5 \cdot 10^{-7}$	$4.5 \cdot 10^{-8}$
1.7	10	1	$4.5 \cdot 10^{-3}$	$1.8 \cdot 10^{-3}$
		2	$1.1 \cdot 10^{-3}$	$4.0 \cdot 10^{-4}$
		5	$1.8 \cdot 10^{-4}$	$7.0 \cdot 10^{-5}$
		10	$4.5 \cdot 10^{-5}$	$1.8 \cdot 10^{-5}$
		15	$2.0 \cdot 10^{-5}$	$7.8 \cdot 10^{-6}$
		20	$1.1 \cdot 10^{-5}$	$4.4 \cdot 10^{-6}$

r_h (AU)	a (mm)	$d_{s/c}$ (km)	Silicates Radiance	Organics Radiance
2.0	0.1	1	$3.5 \cdot 10^{-7}$	$1.3 \cdot 10^{-7}$
		2	$8.8 \cdot 10^{-8}$	$3.3 \cdot 10^{-8}$
		5	$1.4 \cdot 10^{-9}$	$5.2 \cdot 10^{-9}$
		10	$3.5 \cdot 10^{-9}$	$1.3 \cdot 10^{-9}$
		15	$1.5 \cdot 10^{-9}$	$5.8 \cdot 10^{-10}$
		20	$8.8 \cdot 10^{-10}$	$3.3 \cdot 10^{-10}$
2.0	1	1	$4.2 \cdot 10^{-5}$	$1.3 \cdot 10^{-5}$
		2	$1.1 \cdot 10^{-5}$	$3.3 \cdot 10^{-6}$
		5	$1.7 \cdot 10^{-6}$	$5.2 \cdot 10^{-7}$
		10	$4.2 \cdot 10^{-7}$	$1.3 \cdot 10^{-7}$
		15	$1.9 \cdot 10^{-7}$	$5.8 \cdot 10^{-8}$
		20	$1.1 \cdot 10^{-8}$	$3.3 \cdot 10^{-8}$
2.0	10	1	$3.2 \cdot 10^{-3}$	$1.3 \cdot 10^{-3}$
		2	$8.0 \cdot 10^{-4}$	$3.2 \cdot 10^{-4}$
		5	$1.3 \cdot 10^{-4}$	$5.2 \cdot 10^{-5}$
		10	$3.2 \cdot 10^{-5}$	$1.3 \cdot 10^{-5}$
		15	$1.4 \cdot 10^{-5}$	$5.7 \cdot 10^{-6}$
		20	$8.0 \cdot 10^{-6}$	$3.3 \cdot 10^{-6}$

Figure B1: In this table we report the expected spectral radiance of a dust particle, for different combinations of the scattering code parameters. r_h : the heliocentric distance, a: the size of the particles, $d_{s/c}$: the distance of the particle from the spacecraft. Silicates and Organics Radiance are in units of $W/(m^2nm\ sr)$. The refractive index of the silicate material is $m = 1.6 + i10^{-5}$, and the refractive index of the organic material is $m = 1.3 + i10^{-2}$.